

Validation of Computed Extreme Ultraviolet Emission Spectra During Solar Flares

Shohei Nishimoto (✉ ed19004@nda.ac.jp)

National Defense Academy of Japan

Kyoko Watanabe

National Defense Academy of Japan

Toshiki Kawai

Institute for Space-Earth Environmental Research (ISEE), Nagoya University

Shinsuke Imada

Institute for Space-Earth Environmental Research (ISEE), Nagoya University

Tomoko Kawate

National Institute for Fusion Science

Full paper

Keywords: Solar flare, X-ray emission, EUV emission, Space weather

Posted Date: December 7th, 2020

DOI: <https://doi.org/10.21203/rs.3.rs-52084/v2>

License:  This work is licensed under a Creative Commons Attribution 4.0 International License.

[Read Full License](#)

Version of Record: A version of this preprint was published on March 25th, 2021. See the published version at <https://doi.org/10.1186/s40623-021-01402-7>.

- 1 **Title page:**
- 2 **Title:** Validation of Computed Extreme Ultraviolet Emission Spectra During Solar
- 3 Flares
- 4 Shohei Nishimoto, National Defense Academy of Japan, 1-10-20 Hashirimizu,
- 5 Yokosuka 239-8686, Japan, ed19004@nda.ac.jp
- 6 Kyoko Watanabe, National Defense Academy of Japan, 1-10-20 Hashirimizu, Yokosuka
- 7 239-8686, Japan, kwatana@nda.ac.jp
- 8 Toshiki Kawai, Institute for Space-Earth Environmental Research (ISEE), Nagoya
- 9 University, Furo-cho, Chikusa-ku, Nagoya 464-8601, Japan, t.kawai@isee.nagoya-
- 10 [u.ac.jp](mailto:t.kawai@isee.nagoya-u.ac.jp)
- 11 Shinsuke Imada, Institute for Space-Earth Environmental Research (ISEE), Nagoya
- 12 University, Furo-cho, Chikusa-ku, Nagoya 464-8601, Japan, shinimada@isee.nagoya-
- 13 [u.ac.jp](mailto:shinimada@isee.nagoya-u.ac.jp)
- 14 Tomoko Kawate, National Institute for Fusion Science, 322-6 Oroshi-cho, Toki 509-
- 15 5292, Japan, kawate.tomoko@nifs.ac.jp

16 **Abstract**

17 X-rays and extreme ultraviolet (EUV) emissions from solar flares rapidly change the
18 physical composition of the Earth's thermosphere and ionosphere, thereby causing
19 space weather phenomena such as communication failures. To predict the effects of
20 flare emissions on the Earth's upper atmosphere, numerous empirical and physical
21 models have been developed. We verify the extent of reproducing the flare emission
22 spectra using a one-dimensional hydrodynamic calculation and the CHIANTI atomic
23 database. To verify the proposed model, we use the observed EUV spectra obtained by
24 the extreme ultraviolet variability (EVE) on board the Solar Dynamics Observatory
25 (SDO). We examined the "EUV flare time-integrated irradiance" and "EUV flare line
26 rise time" of the EUV emissions for 21 events by comparing the calculation results of
27 the proposed model and observed EUV spectral data. The proposed model succeeded in
28 reproducing the EUV flare time-integrated irradiance of the Fe VIII 131 Å, Fe XVIII 94
29 Å, and Fe XX 133 Å, as well as the 55 to 355 Å and 55 to 135 Å bands. For the EUV
30 flare line rise time, there was acceptable correlation between the proposed model
31 estimations and observations for all Fe flare emission lines. These results demonstrate

32 that the proposed model can reproduce the EUV flare emission spectra from the
33 emitting plasma with relatively high formation temperature. This indicates that the
34 physics-based model is effective for the accurate reproduction of EUV spectral flux.

35

36 **Keywords**

37 Solar flare, X-ray emission, EUV emission, Space weather

38

39 **Main Text**

40 **1. Introduction**

41 To freely utilize outer space as a place for deploying advanced space activities, a
42 common fundamental system, called space infrastructure, is required. To build and use a
43 space infrastructure safely, it is important to accurately grasp the current state of the
44 solar-terrestrial environment, which is strongly influenced by solar activities. Among
45 the solar activities, solar flares have the greatest influence on the solar-terrestrial
46 environment. When solar flares occur, powerful electromagnetic radiation and large
47 amounts of high-energy particles are released. Among these, it is well known that the

48 X-ray and extreme ultraviolet (EUV) emissions of the solar flares, in particular,
49 influence the Earth's communication network. When X-ray and EUV emissions from
50 solar flares reach the Earth's upper atmosphere, especially the D layer of the
51 ionosphere, oxygen and nitrogen in the D layer are ionized. Consequently, the electron
52 density in the D layer increases rapidly, and radio waves (especially at high-frequency
53 ranges) propagating through the D layer are absorbed. This phenomenon is called the
54 Dellinger phenomenon (Dellinger 1937), which is widely known as one of the sudden
55 ionospheric disturbances (SIDs). Solar flare emissions reach the Earth in approximately
56 8 min, and the lead time from solar flare to SIDs is extremely short. Therefore, it is
57 important that the solar irradiance, especially X-ray and EUV emissions, be constantly
58 monitored to minimize the adverse effects of SIDs.

59 In general, it is considered that SIDs are caused by the occurrence of solar flares of the
60 M-class or higher, and can be predicted using the flare class. However, it has been
61 reported that SIDs have occurred from C-class flare, and have not occurred from X-
62 class flares. These observational results suggest that the flare emission contributing to
63 the occurrence of SIDs is not necessarily proportional to the X-ray intensity. To verify

64 what solar flare emission wavelengths influence the occurrence of SIDs, the
65 observational data of the full solar flare emission spectrum is required. However, the
66 spectral observations of EUV and X-ray emissions, which are considered to
67 significantly contribute to SIDs, are limited.

68 X-ray emission has been continuously observed since 1974 by the X-ray Sensors (XRS)
69 on board the Geostationary Operational Environmental Satellite (GOES). GOES/XRS
70 observes two wavelength bands, 0.5 to 4 Å (GOES XRS-A) and 1 to 8 Å (GOES XRS-
71 B) (Bornmann et al. 1996).

72 EUV emission has been observed by different instruments because of its importance
73 form space weather forecasting. The Solar and Heliospheric Observatory (SOHO)
74 satellite, which launched in December 1995, has a Solar EUV Monitor (SEM) (Judge et
75 al. 1998). This instrument has been observing EUV emissions with a 15 s time
76 resolution since January 1996. However, SOHO/SEM only has two wavelength bands,
77 260 to 340 Å and 1 to 500 Å, without wavelength resolution. Hence, only the temporal
78 variation of these EUV emissions can be known from the SOHO/SEM data. The
79 Thermosphere Ionosphere Mesosphere Energetics and Dynamics (TIMED) satellite,

80 which launched in December 2001, has an EUV observation instrument called the Solar
81 EUV Experiment (SEE) (Woods et al. 2005). TIMED/SEE has been observing the
82 wavelength range of 1 to 1940 Å with a 4 Å resolution since January 2002 and has
83 superior spectral resolution compared to SOHO/SEM. However, the time resolution of
84 this is approximately one day, and as such, short-term fluctuations such as solar flares
85 cannot be followed. The Solar Dynamics Observatory (SDO) satellite launched on
86 February 2010 includes the Extreme Ultraviolet Variability Experiment (EVE) (Woods
87 et al. 2012). The Multiple EUV Grating Spectrograph (MEGS), a subsystem of the
88 SDO/EVE, has measured full disk solar irradiance in the 1 to 1060 Å range with 1 Å
89 spectral resolution and a 10 s time cadence since May 2010. MEGS-A observes the
90 wavelength range 50 to 370 Å, and MEGS-B observes the wavelength range 350 to
91 1050 Å. MEGS-A was the only instrument that could observe throughout the day with
92 sufficient spectral and temporal resolution to study the EUV flare emission spectra;
93 however, this device was terminated in May 2014 owing to a charge-coupled device
94 (CCD) power anomaly. Although MEGS-B remains in operation today, it is possible
95 that a flare is not observed because MEGS-B can only operate for approximately three

96 hours a day. Therefore, the observation of high-resolution EUV emission spectra when
97 a solar flare occur is not guaranteed.

98 To model the emission spectra, we must understand the emission mechanism in solar
99 flares. The basic conceptual model for solar flares is the CSHKP model (Carmichael
100 1964; Sturrock 1966; Hirayama 1974; Kopp & Pneuman 1976; Yokoyama & Shibata
101 1998; Shiota et al. 2005). According to this model, solar flares are caused by “magnetic
102 reconnection” generated in the solar corona (Innes et al. 2003; Imada et al. 2013;
103 Warren et al. 2018). The strong magnetic tension generated by the magnetic
104 reconnection heat accelerates the electrons or protons in the solar corona. The
105 accelerated particles travel downward along the magnetic field lines, fall into the
106 chromosphere, and rapidly heat the high-density plasma. The high-temperature and
107 high-density plasmas rise from the chromosphere along the magnetic field lines and
108 form a loop-shaped structure; this phenomenon is called “chromospheric evaporation”
109 (Milligan & Dennis 2009; Imada et al. 2015; Lee et al. 2017). The loop structure
110 observed by soft X-ray and EUV formed from chromospheric evaporation is called the
111 “flare ribbon”. Soft X-ray and EUV emissions are emitted from the flare loop. The time

112 evaporation of the EUV emissions is characterized by the formation temperature of the
113 emitting plasmas. A typical flare light curve of an EUV emission has as impulsive peak
114 at the beginning, followed by a gradual peak, called the impulsive and gradual phases,
115 respectively. In general, the relatively cooler EUV line emissions from the plasma
116 below the transition region are observed in the impulsive phase corresponding to the
117 rapid heating in the early stages of chromospheric evaporation, and hotter EUV line
118 emissions are observed in the gradual phase corresponding to the radiative cooling of
119 the flare loop. Therefore, the emission spectra are evidently different between the
120 impulsive and gradual phases because their origins are different.

121 Different flare EUV emission prediction models have been constructed based on the
122 above flare emission mechanism. The most widely used model is the Flare Irradiance
123 Spectral Model (FISM) (Chamberlin et al. 2006, 2007, 2008). The FISM is an empirical
124 model that derives EUV emission spectra using the GOES soft X-ray flux observation.
125 The FISM estimates the wavelength range of 1 to 1900 Å with 10 Å spectral resolution
126 and 60 s cadence. It has been reported that the FISM can accurately estimate the solar
127 flare emission spectra within 40% for a wavelength in the range 140 to 1900 Å.

128 However, FISM has low accuracy on wavelengths less than 140 \AA ; this is the
129 wavelength range containing the EUV emission lines that are mainly enhanced during
130 the gradual phase of a flare. This is because the FISM considers the time evolution of all
131 EUV line emissions to be the same as the time evolution of the soft X-ray during the
132 flare, and the cooling of the flare loop (time difference of EUV line emissions) is not
133 well represented. Consequently, the FISM under predicts the flare duration and
134 deposited energy (Thiemann et al. 2017).

135 The Q_{EUV} , for which the 0 to 450 \AA EUV band is an important indicator for the EUV
136 irradiance input to the Earth's upper atmosphere (Strickland 1995), and the EUV
137 irradiance in the 0 to 70 \AA and 70 to 170 \AA bands have the greatest contribution to the
138 Q_{EUV} (Woods et al. 2011). Therefore, EUV irradiance from wavelengths less than 140
139 \AA is important. To solve this discrepancy, it is necessary to estimate the time evolution
140 of the EUV emissions accurately.

141 Other physical-based models have been constructed for this purpose; however, the EUV
142 emission was only partially reproduced (Li et al. 2014; Zeng et al. 2014). Thiemann et
143 al. (2017) partially succeeded in modeling the timing to coronal loop cooling with an

144 empirical rule. These studies used a zero-dimensional hydrodynamic model to simulate
145 the thermal evolution of the coronal loops, called the enthalpy-based thermal evolution
146 of loops (EBTEL) model, that could calculate the temperature and density in the flare
147 loop without calculating the spatial loop evolution (Klimchuk et al. 2008; Cargill et al.
148 2012). The EBTEL model did not calculate the spatial distribution of the emitting
149 plasma in the flare loop; hence, it is possible that the emission from the transition region
150 plasma would not be reproduced accurately (Kawai et al. 2020). Kawai et al. (2020)
151 introduced a new method for reproducing EUV flare emission spectra considering the
152 time evolution of the plasma distribution in the flare loop. This method was constructed
153 using a one-dimensional hydrodynamic calculation and an atomic database. The details
154 of the method are described in Section 3 and 4.

155 In this paper, we present the statistical results of the EUV emission spectra observed by
156 SDO/EVE for 21 flare events and compare these with the spectra reproduced by Kawai
157 et al. (2020)'s method. The purpose of this study is to investigate the accuracy in
158 reproducing solar flare emission spectra using a simple method based on the physics of
159 flare loops and to examine the important parameters for reproducing the solar flare

160 emissions.

161 The remainder of the paper consists of following sections. Section 2 presents the
162 extraction of the comparative parameters using GOES and SDO/EVE. Section 3
163 introduces the models used in this study. Section 4 presents an example of the
164 derivation of the solar flare emission spectra using the proposed model. Section 5
165 presents the statistical results of the comparison between the proposed model
166 simulations and observations and verifies the solar flare emission spectra. Section 6
167 discusses and summarizes the presented comparison results.

168

169 **2. Data**

170 **2.1 Soft X-ray observation**

171 we used the soft X-ray data observed by the GOES/XRS. Flare class and duration are
172 typically determined with GOES XRS-B light curve observations. In this study, the
173 flare start, peak, and end times were defined using the time derivative data of the GOES
174 XRS-B light curve observations to not lose the impulsive and gradual phases.
175 Furthermore, we divided the flare duration into the rise time and decay time to

176 investigate the flare evolution in detail. Figure 1 displays an example of determining the
177 rise time and decay time for the M9.9-class flare on January 1, 2014. The rise time is
178 determined by when the positive derivative value is observed continuously from the
179 GOES XRS-B start time to the peak time. The decay time is determined by when the
180 negative derivative value is observed continuously from the GOES XRS-B peak time to
181 the end time.

182 **2.2 EUV flare emission spectra observation**

183 we examined the EUV emission spectra obtained from the SDO/EVE MEGS-A
184 observations. For this study, we selected flare events greater than M3-class flare that
185 occurred between November 2010 and May 2014 from the Hinode flare catalogue
186 (Watanabe et al. 2012). We used 21 events observed by the SDO/EVE MEGS-A during
187 this period.

188 Figure 2 displays the EUV spectrum at flare peak time (18:52 UT) for the M9.9-class
189 flare on January 1, 2014 observed by the SDO/EVE MEGS-A. This EUV spectrum was
190 subtracted non-enhanced value (18:00 UT) from the spectral value of each wavelength
191 before the flare as background. We focused on the six EUV flare lines of Fe VIII 131 Å,

192 Fe XV 284 Å, Fe XVI 335 Å, Fe XVIII 94 Å, Fe XX 133 Å, and He II 304 Å, which
193 were strongly enhanced during the flare. The formation temperature of the Fe XX 133 Å
194 is ~ 9 to 13 MK, Fe XVIII 94 Å is ~ 6 MK, Fe XVI 335 Å is ~ 3 MK, Fe XV 284 Å is ~
195 2 MK, Fe VIII 131 Å is ~ 0.4 MK, and He II 304 Å is ~ 0.05 MK. Figure 3 displays the
196 EUV light curves of these six flare lines during M9.9-class flare on January 1, 2014. We
197 subtracted the 3 min average value during the non-enhanced around top of the hour
198 before the flare start for each line flux. Furthermore, we used 110 s as the running
199 average to remove the noise due to short term fluctuations (dashed line in Figure 3).
200 To investigate the flare deposited energy and duration, which have a significant
201 influence on the Earth's thermosphere and ionosphere response (Qian et al. 2011), we
202 extracted the "EUV flare time-integrated irradiance" and the "EUV flare line rise time"
203 as comparison parameters.
204 The EUV flare time-integrated irradiance is the time-integrated value of the irradiance
205 from the flare start to end time. We examined for EUV flare lines 55 to 355 Å and 55 to
206 135 Å band. The wavelength band of 55 to 135 Å, where the uncertainty of the FISM
207 calculation is considerable and significantly influences the Earth's ionosphere (Woods

208 et al. 2011; Thiemann et al. 2017). This relatively short wavelength band consists of the
209 hot EUV lines and dominates the EUV emissions in the gradual phase (Woods et al.
210 2011). The EUV flare rise time is the duration from the flare start to EUV line peak
211 time as with the above mentioned soft X-ray observation.

212

213 **3. Models**

214 **3.1 Coordinated Astronomical Numerical Software (CANS) 1D package**

215 We used the one-dimensional hydrodynamic model called CANS 1D package
216 ([http://www-space.eps.s.u-
tokyo.ac.jp/~yokoyama/etc/cans/index-e.html](http://www-space.eps.s.u-tokyo.ac.jp/~yokoyama/etc/cans/index-e.html)) to solve the
217 physical process of the plasma in the flare loop. This package can calculate the energy
218 redistribution process in the flare loop that occurs after the energy input. The simulation
219 set up in this package is the same as Hori et al. (1997) or Imada and Zweibel. (2012).

220 CANS 1D simulates one-dimensional fluid motion and energy transfer along an
221 invariant magnetic loop. It assumes that the cross section of the magnetic loop does not
222 change in time. The fluid was considered as non-viscous and compressible and included
223 heat conduction and radiative cooling. Gravity was also considered. The fundamental

224 equations of CANS 1D are as follows:

$$225 \quad \frac{\partial}{\partial t}(\rho S) + \frac{\partial}{\partial x}(\rho V_x S) = 0 \quad (1)$$

$$226 \quad \frac{\partial}{\partial t}(\rho V_x S) + \frac{\partial}{\partial x}[(\rho V_x^2 + p)S] = \rho g S \quad (2)$$

$$227 \quad \frac{\partial}{\partial t} \left[\left(\frac{p}{\gamma - 1} + \frac{1}{2} \rho V_x^2 \right) S \right] + \frac{\partial}{\partial x} \left[\left(\frac{\gamma}{\gamma - 1} p + \frac{1}{2} \rho V_x^2 \right) V_x S - \kappa \frac{\partial T}{\partial x} S \right] = (\rho g V_x + H - R + H_f) S \quad (3)$$

$$228 \quad p = \frac{k_B}{m} \rho T \quad (4)$$

229 where ρ is the plasma density, S is the cross section, V_x is the plasma velocity, g is

230 the gravitational acceleration, $\gamma = 5/3$ is the specific heat ratio, κ is the thermal

231 conductivity coefficient, H is the static heating, R is the radiative cooling, H_f is the

232 flare heating term, k_B is the Boltzmann constant, and m is the mean particle mass.

233 The Spitzer model was used as the thermal conductivity coefficient (Spitzer 1962). The

234 calculation region is from the foot point of the flare loop, which means the photosphere

235 ($x = 0$) to the flare loop top ($x = L$), where L is the half-loop length.

236 Flare heating is given as a function of time and space, as follows:

$$237 \quad H_f = H_{f0} \cdot q(t) \cdot f(x) \quad (5)$$

$$238 \quad q(t) = \frac{1}{4} \left\{ 1 + \tanh \frac{t}{0.1\tau_0} \right\} \left\{ 1 - \tanh \frac{t - \tau_f}{0.1\tau_0} \right\} \quad (6)$$

$$239 \quad f(x) = \frac{1}{\sqrt{2\pi}} \exp \left[-\frac{(x - L)^2}{2w_f^2} \right] \cdot \frac{1}{2} \left\{ 1 + \tanh \left(\frac{x - 20\mathcal{H}_0}{3\mathcal{H}_0} \right) \right\} \quad (7)$$

240 where H_{f0} is the input energy, τ_f is the heating duration, and w_f is the heating
241 width. \mathcal{H}_0 is the scale height at the photosphere ($x = 0$).

242 **3.2 CHIANTI atomic database**

243 We used the CHIANTI atomic database to reproduce the X-ray and EUV emissions
244 originating from the flare loop. The CHIANTI database contains a large amount of
245 atomic data for the analysis of astrophysical spectra including atomic energy levels,
246 wavelengths, radiative transition probabilities, rate coefficients for ionization, and data
247 to calculate different emissions (Dere et al. 1997).

248

249 **4. Validation of M9.9-class flare on January 1, 2014**

250 We compared the EUV flare time-integrated irradiance and EUV flare line rise time
251 obtained from the proposed model and SDO/EVE MEGS-A observations. The model
252 simulations were in accordance with Kawai et al. (2020). This model simulations
253 can reproduce the EUV spectrum by using CANS 1D and CHIANTI atomic
254 database. We calculate the GOES XRS-B light curve when flare occurs in the
255 simulation. Then, we convert it to observed one by stacking it with matching these

256 peaks. The EUV dynamic spectrum can be calculated by converting it as same as XRS-
257 B.

258 **4.1 Preprocessing**

259 As a preparation to simplify the derivation of the EUV emission spectrum, the rise and
260 decay time were fit to exponential curves using the Gauss-Newton method (see the
261 section 3.1 in Kawai et al. (2020)). Figure 4 displays an example of the fit GOES XRS-
262 B light curve for the M9.9-class flare on January 1, 2014.

263 **4.2 Coronal loop length measurement**

264 The flare loop length for the parameter used in CANS 1D was estimated by the
265 observation of the separation distance of the ribbons, called ribbon distance, with the
266 SDO/Atmospheric Imaging Assembly (AIA) (Lemen et al. 2012). We used 1600 Å
267 images to obtain the ribbon distance immediately before the flare start. Before deriving
268 the ribbon distance, we corrected the projection effect by rotating the flaring region to
269 the solar center using the solar software `drot_map.pro`. First, we defined the flare ribbon
270 as a region with intensities of 40 times greater than the standard deviation of the quiet
271 region. Ribbon distance is derived as the distance between the two brightest points in

272 the flare ribbons and is known as the $H\alpha$ (UV) kernel (Asai et al. 2003; Temmer et al.
273 2007). For the M9.9-class flare on January 1, 2014, as indicated in Figure 5, the ribbon
274 distance was derived as 23.3 arcsec. Therefore, the ribbon distance of this event was
275 estimated to be 16.9 Mm. Subsequently, the loop length was estimated to be 26.5 Mm
276 by assuming a semicircle whose diameter was this ribbon distance.

277 **4.3 Numerical simulation**

278 We reproduced the time evolution of the plasma in the flare loop with CANS 1D as
279 described in Section 3.1. Figure 6 displays an example of the calculated results of
280 CANS 1D. In this case, we set L to 26.5 Mm, H_{f0} was $6.0 \text{ erg cm}^{-3} \text{ s}^{-1}$, w_f was
281 600 km, and τ_f was 240 s (Equations (5) - (7)). We determined L from the
282 observation of the ribbon distance described in section 4.2, w_f and τ_f were from the
283 default parameter values of CANS 1D (see the CANS 1D documentation), and H_{f0}
284 was chosen arbitrarily and the magnitude of the computed GOES XRS-B light curve are
285 scaled to better match the observation. From the result, we identified the transition
286 region to be near 0.3 Mm. In the figure, the temperature and density in the flare loop
287 rise sharply in a couple of hundred seconds and at a height of 0.3 Mm, and the edge

288 moves temporally. This represents the evolution of chromospheric evaporation. When
289 flare occurs, accelerated particles fall on the chromosphere along the magnetic field
290 lines. Consequently, the low temperature plasma in the chromosphere is rapidly heated
291 and transported upward owing to the pressure gradient. Hence, this calculation can
292 reproduce the time evolution of the plasma in the flare loop.

293 **4.4 Conversion from GOES X-ray to EUV spectrum**

294 We calculated the temporal variation and distribution of temperature, density, pressure,
295 and plasma velocity of emitting plasma in the single loop using CANS 1D (shown in
296 Figure 6). Then, we derived the synthetic emissions corresponding to the CANS 1D
297 results using CHIANTI atomic database version 9.0 (Dere et al. 2019). The abundance
298 file used in this study is “sun_coronal_2012_schmelz” (see section 3.4 in Kawai et al.
299 (2020)). Finally, we converted the synthetic flare emissions into a light curve that was
300 comparable to the observation (see section 3.5 in Kawai et al. (2020)). Figure 7 displays
301 the reproduced GOES XRS-B light curve by the proposed model. We performed the
302 conversion as follows using the fit GOES XRS-B light curve as described above. First,
303 we calculated the ratio between the GOES XRS-B observation and simulated GOES

304 XRS-B light curve (simply integrated calculated value of 1 to 8 Å) for each observation
305 time. Afterwards, we performed convolution on the simulated GOES XRS-B light curve
306 with the observation. Subsequently, we calculated the ratio between the maximum value
307 of the GOES XRS-B observation and maximum value of the convoluted GOES XRS-B
308 light curve. We applied these two ratios to all simulated light curves. Finally, we
309 derived the EUV emission spectra in all wavelengths that was comparable to the
310 observation (see Fig. 1 in Kawai et al. (2020)). Previous studies have reported that flare
311 emission is well reproduced by reproducing the time evolution of multiple flare loops
312 (e.g. Hori et al. (1997); Reep and Toriumi. (2017)). The method of convolving a simple
313 calculation for single loop into the GOES X-ray observation proposed by Kawai et al.
314 (2020) can roughly reproduced pseudo emission from multiple flare loops, and at the
315 same time, can reduce computational complexity and cost.

316 Figure 8 displays an example of the EUV flare time-integrated spectra during the M9.9-
317 class flare on January 1, 2014. The dashed red, blue, and solid green lines indicate the
318 values obtained from the proposed model, FISM, and SDO/MEGS-A observations,
319 respectively. As indicated in Figure 8, both the proposed model and FISM reproduced

320 the tendency of the observed values. Owing to the superior wavelength resolution, the
321 proposed model reproduced each EUV flare line, which was not represented by the
322 FISM. Figure 9 displays the light curves of the EUV flare lines observed by SDO/EVE
323 MEGS-A (top panel), estimated by the proposed model (middle panel), and the FISM
324 (bottom panel) for the M9.9-class flare on January 1, 2014. The wavelength resolution
325 of these light curves was 10 \AA , which was the same as FISM. Therefore, the wavelength
326 of Fe VIII and Fe XX is 130 \AA , Fe XV is 280 \AA , Fe XVI is 330 \AA , Fe XVIII is 90 \AA ,
327 and He II is 300 \AA as indicated in Figure 9. It is clear that the proposed model can
328 reproduce the flux of each line based on the formation temperature. Conversely, the
329 light curves of the FISM were virtually the same as the Fe XX observation of
330 SDO/EVE MEGS-A, regardless of the lines or events. Table 1 presents the EUV flare
331 time-integrated irradiance and EUV flare line rise time, observed by SDO/EVE MEGS-
332 A and calculated by the proposed model for the M9.9-class flare on January 1, 2014,
333 respectively.

334

335 **5. Statistical study for comparison between model and observation**

336 We compared the EUV flare time-integrated irradiance and EUV flare line rise time
337 obtained from the proposed model and SDO/EVE MEGS-A observation for 21 flare
338 events using the same method as the event analysis in Section 4.

339 In this study, we used the default parameter values set in CANS 1D (see the CANS 1D
340 documentation). Afterwards, we set the optimal input energy for each flare event as a
341 variable parameter (see the equations (5) - (7)). The GOES classes, flare dates, times,
342 half-loop length estimations from the SDO/AIA observation, and the input energy used
343 in the proposed model for 21 flare events are presented in Table 2.

344 First, we compared the flare time-integrated irradiance of each EUV line. Figure 10
345 displays the correlation of the EUV flare time-integrated irradiance of six flare lines. All
346 Fe lines have acceptable correlation with the observations. However, the He II indicates
347 poor correlation with the correlation coefficient of 0.24 (Figure 10f). As indicated in the
348 regression lines in Figure 10, the Fe XVIII (Figure 10d) effectively reproduced the
349 observed data. Fe XV (Figure 10b) and Fe XVI (Figure 10c) tended to be
350 overestimated; the Fe VIII (Figure 10a), Fe XX (Figure 10e), and He II (Figure 10f)
351 lines tended to be underestimated by the proposed model.

352 Afterwards, we compared the flare energies for two wavelength bands.

353 Figure 11 displays the comparison results of the EUV flare time-integrated irradiance of

354 two wavelength bands of 55 to 355 Å (Figure 11a) and 55 to 135 Å (Figure 11b). The

355 results of the proposed model and FISM are plotted in red and blue, respectively. As

356 indicated in Figure 11a, the 55 to 355 Å band was well reproduced by both the proposed

357 model and FISM. The slopes of the regression lines were 0.81 ± 0.08 and 1.22 ± 0.02 ,

358 respectively, and the correlation coefficients were 0.92 and 0.99, respectively.

359 Moreover, for the 55 to 135 Å band, the proposed model could reproduce the

360 observations better than the FISM (Figure 11b). From Figure 11b, the slope of the

361 regression line for the proposed model was 0.91 ± 0.08 , and the correlation coefficient

362 was 0.94. Conversely, the slope of the regression line for the FISM was 0.53 ± 0.01 , and

363 the correlation coefficient is 0.99. From these results, the FISM tended to underestimate

364 the EUV flare time-integrated irradiance at this relatively shorter wavelength band.

365 Figure 12 displays the comparison results of the EUV flare line rise time statistically.

366 The correlation coefficient of the Fe VIII was 0.95 (Figure 12a), Fe XV was 0.86

367 (Figure 12b), Fe XVI was 0.90 (Figure 12c), Fe XVIII was 0.92 (Figure 12d), Fe XX

368 was 0.94 (Figure 12e), and He II was 0.80 (Figure 12f). It can be clearly observed that
369 all Fe lines indicated acceptable correlations with the observations. From these scatter
370 plots, the calculated rise time of Fe XV, Fe XVI, and Fe XX tended to be less than the
371 observations (Figure 12b, c, e), whereas He II tended to be greater than the observations
372 (Figure 12f).

373

374 **6. Discussion and summary**

375 We attempted to reproduce EUV flare emission spectra using a simple physics-based
376 model that simulates the time evolution of emitting plasma distribution in the flare loop.
377 We verified the EUV flare time-integrated irradiance and EUV flare line rise time of
378 EUV line emissions for 21 events by comparing the calculation results of the proposed
379 model and observed EUV spectral data.

380 For the flare time-integrated irradiance, the proposed model succeeded in reproducing
381 the Fe VIII, Fe XVIII, and Fe XX lines (Figure 10a, d, e) as well as the 55 to 355 Å and
382 55 to 135 Å band (Figure 11a). Our results indicate that the physics-based model was
383 effective in reproducing EUV flare irradiance for wavelengths less than 140 Å.

384 Conversely, the proposed model overestimated the relatively longer wavelength lines,
385 Fe XV and Fe XVI lines, emitted from relatively cooler plasmas (Figure 10b, c).

386 Thiemann et al. (2018) reported that the peak EUV irradiance of emission lines with
387 higher formation temperatures (> 9 MK) is proportional to the GOES XRS-B peak
388 emission measure. Therefore, our results could imply that the EUV irradiance of the
389 emitting plasmas with a lower formation temperature are not linearly proportional to the
390 irradiance of the hotter emission lines or soft X-ray flux.

391 Regarding the EUV flare line rise time, the proposed model could derive the time
392 evolution of the EUV line emission by simulating the time evolution of the temperature
393 in the flare loop. This tendency can be observed from the fact that the difference of peak
394 time depending on the formation temperature of the emitting plasma was reproduced by
395 the proposed model as indicated in Figure 9. The Fe XX line, which was emitted from
396 the highest formation temperature plasma, had the shortest rise time (Figure 12d), and
397 the He II line, which emitted from the lowest formation temperature, had the longest
398 rise time (Figure 12f). This is because the time evolution of each EUV flare line is
399 determined by the temperature of the emitting plasma in the proposed model.

400 For the He II emission line, both the time-integrated irradiance (Figure 10f) and EUV
401 flare line rise time (Figure 12f) were poorly reproduced by the proposed model. This is
402 because the proposed model neglected the EUV emissions from below the transition
403 region, which is the origin of the optically thick plasmas, and hence, we did not
404 calculate the radiation transfer. The proposed model is based primarily on the physical
405 process following the soft X-ray emission. Therefore, a future work is to construct a
406 model that can accurately reproduce the EUV emission from optically thick plasmas
407 that are dominant in the impulsive phase.

408 In this study, we used, for the most part, the default parameter values set in the CANS
409 1D (see the CANS 1D documentation). Then, we used the half-loop length estimated
410 from observation, and set the optimal input energy for each flare event as a variable
411 parameter. These parameters are listed in Table 2. Our results indicate that the EUV
412 emissions from emitting plasma with relatively high formation temperature could be
413 reproduced using only the flare input energy as a variable parameter.

414 As mentioned above, our results indicate that the physics-based model is effective for
415 reproducing EUV flare emissions. The proposed model succeeded in reproducing not

416 only the EUV emission intensity of Fe lines with high formation temperature but also
417 the time evolution of all Fe lines during a flare. Because the Earth's ionosphere and
418 thermosphere are sensitive to EUV emissions from the Sun (Qian et al. 2011), an
419 accurate estimation of the EUV irradiance and duration during solar flares is important
420 from the viewpoint of space weather. Therefore, we consider that the simple model used
421 in this study can contribute to the space weather forecast operation.

422

423 **Declarations**

424 **Ethics approval and consent to participate**

425 No applicable

426 **Consent for publication**

427 No applicable

428 **List of abbreviations**

429 **AIA:** Atmospheric Imaging Assembly

430 **CANS:** Coordinated Astronomical Numerical Software

431 **CC:** Correlation Coefficient

432 **CCD:** Charge-Coupled Device

433 **EBTEL:** Enthalpy-Based Thermal Evolution of Loops

434 **EUV:** Extreme Ultraviolet

435 **EVE:** Extreme Ultraviolet Variability Experiment

436 **FISM:** Flare Irradiance Spectral Model

437 **GOES:** Geostationary Operational Environmental Satellite

438 **MEGS:** Multiple EUV Grating Spectrograph

439 **SEE:** Solar EUV Experiment

440 **SEM:** Solar EUV Monitor

441 **SDO:** Solar Dynamics Observatory

442 **SIDs:** Sudden Ionospheric Disturbances

443 **SOHO:** Solar and Heliospheric Observatory

444 **TIMED:** Thermosphere Ionosphere Mesosphere Energetics and

445 Dynamics

446 **UV:** ultraviolet

447 **UT:** universal time

448 **XRS: X-ray Sensors**

449

450 **Availability of data and materials**

451 The SDO/EVE level 2 data version 6 data are available at

452 http://lasp.colorado.edu/eve/data_access/eve_data/products/level2/. FISM

453 data are available at https://lasp.colorado.edu/lisird/data/fism_flare_hr/.

454 The flare event data used in this study can be found in Hinode flare

455 catalogue (https://hinode.isee.nagoya-u.ac.jp/flare_catalogue/).

456 **Competing interests**

457 The authors declare that they have no competing interests.

458 **Funding**

459 Part of this work was conducted by the joint research program of the

460 Institute for Space-Earth Environmental Research (ISEE), Nagoya

461 University. This study was supported by JSPS KAKENHI Grant

462 Numbers JP16H01187, and JP18H04452.

463 **Authors' contributions**

464 SN performed statistical study for solar flare spectrum data and drafted
465 the manuscript. KW, TK, SI and TK discussed the results and edited the
466 manuscript. All authors read and approved the final manuscript.

467 **Acknowledgements**

468 The authors would like to thank to K. Ichimoto, S. Takasao, S. Toriumi,
469 H. P. Warren, and J. W. Reep for stimulating fruitful discussions.

470 **References**

471 Asai, A., Ishii, T. T., Kurokawa, H., Yokoyama, H., Shimojo, M. (2003) Evolution Of
472 Conjugate Footpoints Inside Flare Ribbons During A Great Two-Ribbon Flare On
473 2001 April 10, *Astrophysical Journal*, 586:624-629.

474 Bornmann, P. L., Speich, D., Hirman, J., et al. (1996) GOES X-ray sensor and its use in
475 predicting solar-terrestrial disturbances, *Proceedings of SPIE*, 2812:291-298.

476 Cargill, P. J., Bradshaw, S. J., Klimchuk, J. A. (2012) Enthalpy-based Thermal
477 Evolution of Loops. III. Comparison of Zero-dimensional Models, *Astrophysical*
478 *Journal*, 758:5.

479 Carmichael, H. (1964), A Process for Flares, *Proceedings of the AAS-NASA*

480 Symposium, 50:451.

481 Chamberlin, P. C., Woods, T. N., Eparvier, F. G. (2006) Flare Irradiance Spectral
482 Model (FISM) use for space weather applications, Proceedings of the ILWS
483 Workshop, 153.

484 Chamberlin, P. C., Woods, T. N., Eparvier, F. G. (2007) Flare Irradiance Spectral
485 Model (FISM): Daily component algorithms and results, Space Weather, 5:S07005,
486 <https://doi.org/10.1029/2007SW000316>

487 Chamberlin, P. C., Woods, T. N., Eparvier, F. G. (2008) Flare Irradiance Spectral
488 Model (FISM): Flare component algorithms and results, Space Weather, 6:S05001,
489 <https://doi.org/10.1029/2007SW000372>

490 Dellinger, J. H. (1937) Sudden disturbances of the ionosphere, Journal of Applied
491 Physics, 8:32-751.

492 Dere, K. P., Landi, E., Mason, H. E., Monsingnori, B. C., Young, P. R. (1997)
493 CHIANTI - an atomic database for emission lines, Astronomy & Astrophysics
494 Supplement, 125:149-173.

495 Dere, K. P., Zanna, G. D., Young, P. R., Landi, E., Sutherland, R. S. (2019) CHIANTI –

496 AN Atomic Database for Emission Lines. XV. Version 9, Improvements for the X-
497 Ray Satellite Lines, *Astrophysical Journal Supplement*, 241:22.

498 Hirayama, T. (1974) Theoretical Model of Flares and Prominences. I: Evaporating Flare
499 Model, *Solar Physics*, 34:323-338.

500 Hori, K., Yokoyama, T., Kosugi, T., Shibata, K. (1997) Pseudo-Two-Dimensional
501 Hydrodynamic Modeling Of Solar Flare Loops, *Astrophysical Journal*, 489:426-441

502 Imada, S., Zweibel, E. G. (2012) Self-Organization Of Reconnecting Plasma To
503 Marginal Collisionality In The Solar Corona, *Astrophysical Journal*, 755:93

504 Imada, S., Aoki, K., Hara, H., Watanabe, T., Harra, L. K., Shimizu, T. (2013) Evidence
505 for Hot Fast Flow above a Solar Flare Arcade, *Astrophysical Journal Letters*,
506 776:L11.

507 Imada, S., Murakami, I., Watanabe, T. (2015) Observation and numerical modeling of
508 chromospheric evaporation during the impulsive phase of a solar flare, *Physics of*
509 *Plasmas*, 22:101206, <https://doi.org/10.1063/1.4932335>

510 Innes, D. E., McKenzie, D. E., Wang, T. J. (2003) Observations of 1000 km s^{-1}
511 Doppler shifts in 10^7 K solar flare supra-arcade, *Solar Physics*, 217:267-279.

512 Judge, D. L., McMullin, D. R., Ogawa, H. S., et al. (1998) First Solar EUV Irradiances
513 Obtained from SOHO by the CELIAS/SEM, *Solar Physics*, 177:161-173.

514 Kawai, T., Imada, S., Nishimoto, S., Watanabe, K., Kawate, T. (2020) Nowcast of an
515 EUV dynamic spectrum during solar flares. *Journal of Atmospheric and Solar-*
516 *Terrestrial Physics*, 205:105302.

517 Klimchuk, J. A., Patsourakos, S., Cargill, P. J. (2008) Highly Efficient Modeling of
518 Dynamic Coronal Loops, *Astrophysical Journal*, 682:1351-1362.

519 Kopp, R. A., Pneuman, G. W. (1976) Magnetic reconnection in the corona and the loop
520 prominence phenomenon, *Solar Physics*, 50:85-98.

521 Lee, K. S., Imada, S., Watanabe, K., Bamba, Y., Brooks, D. H. (2017) IRIS, Hinode,
522 SDO, and RHESSI Observations of a White Light Flare Produced Directly by
523 Nonthermal Electrons, *Astrophysical Journal*, 836:150.

524 Lemen, J. R., Title, A. M., Boerner, P. F., et al. (2012) The Atmospheric Imaging
525 Assembly (AIA) on the Solar Dynamics Observatory (SDO), *Solar Physics*, 275:17-
526 40.

527 Li, Y., Qiu, J., Ding, M. (2014) Heating and Dynamics of Two Flare Loop Systems

528 Observed by AIA and EIS, *Astrophysical Journal*, 781:120.

529 Milligan, R. O., Dennis, B. R. (2009) Velocity Characteristics of Evaporated Plasma
530 Using Hinode/EUV Imaging Spectrometer, *Astrophysical Journal*, 699:968-975.

531 Qian, L., Burns, A. G., Chamberlin, P. C., Solomon, S. C. (2011) Variability of
532 thermosphere and ionosphere responses to solar flares, *Journal of Geophysical
533 Research: Space Physics*, 116:A10309, <https://doi.org/10.1029/2011JA016777>

534 Reep, J. W., Toriumi, S. (2017) The Direct Relation between the Duration of Magnetic
535 Reconnection and the Evolution of GOES Light Curves in Solar Flares,
536 *Astrophysical Journal*, 851:4.

537 Shiota, D., Isobe, H., Chen, P. F., Yamamoto, T., Sakajiri, T., Shibata, K. (2005) Self-
538 Consistent Magnetohydrodynamic Modeling of a Coronal Mass Ejection, Coronal
539 Dimming, and a Giant Cusp-shaped Arcade Formation, *Astrophysical Journal*,
540 634:663-678.

541 Spitzer, L. (1962) *Physics of Fully Ionized Gases*, Interscience Publishers, New York.

542 Strickland, D. J., Evans, F. S., Paxton, L. J. (1995) Satellite remote sensing of
543 thermospheric O/N₂ and solar EUV: 1. Theory, *Journal of Geophysical Research*,

544 100:12217-12226.

545 Sturrock, P. A. (1966) Model of the High-Energy Phase of Solar Flares, *Nature*

546 211:695-697.

547 Temmer, M., Veronig, A. M., Vršnak, B., Miklenic, C. (2007) Energy Release Rates

548 Along Ha Flare Ribbons And The Location Of Hard X-Ray Sources, *Astrophysical*

549 *Journal*, 654:665-674.

550 Thiemann, E. M. B., Eparvier, F. G., Woods, T. N. (2017) A time dependent relation

551 between EUV solar flare light-curves from lines with differing formation

552 temperatures, *Journal of Space Weather and Space Climate*, 7:A36,

553 <https://doi.org/10.1051/swsc/2017037>.

554 Thiemann, E. M. B., Chamberlin, P. C., Eparvier, F. G., Epp, L. (2018) Center-to-Limb

555 Variability of Hot Coronal EUV Emissions During Solar Flares, *Solar Physics*,

556 293:19.

557 Warren, H. P., Brooks, D. H., Ugarte-Urra, I., et al. (2018) Spectroscopic Observations

558 of Current Sheet Formation and Evolution, *Astrophysical Journal*, 854:122.

559 Watanabe, K., Masuda, S., Segawa, T. (2012) Hinode Flare Catalogue, *Solar Physics*,

560 279:317-322.

561 Woods, T. N., Eparvier, F. G., Bailey, S. M., et al. (2005) Solar EUV Experiment
562 (SEE): Mission overview and first results, *Journal of Geophysical Research: Space*
563 *Physics*, 110:A01312, <https://doi.org/10.1029/2004JA010765>

564 Woods, T. N., Hock, R., Eparvier, F. G., et al. (2011) New Solar Extreme-ultraviolet
565 Irradiance Observations during Flares, *Astrophysical Journal*, 739:59.

566 Woods, T. N., Eparvier, F. G., Hock, R., et al. (2012) Extreme Ultraviolet Variability
567 Experiment (EVE) on the Solar Dynamics Observatory (SDO): Overview of Science
568 Objectives, Instrument Design, Data Products, and Model Developments, *Solar*
569 *Physics*, 275:115-143.

570 Yokoyama, T., Shibata, K. (1998) A Two-dimensional Magnetohydrodynamic
571 Simulation of Chromospheric Evaporation in a Solar Flare Based on a Magnetic
572 Reconnection Model, *Astrophysical Journal*, 494:L113-L116.

573 Zeng, Z., Qiu, J., Cao, W., Judge, P. G. (2014) A Flare Observed in Coronal, Transition
574 Region, and Helium I 10830 Å Emissions, *Astrophysical Journal*, 793:87.

575

576 **Figure legends Table Legends**

577 Figure 1. Example of GOES XRS-B observation.

578 The light curve of soft X-ray flux (1 to 8 Å) observed by the GOES XRS-B for the
579 M9.9-class flare on January 1, 2014 (upper panel). The light curve of the soft X-ray
580 time derivative flux (lower panel). The vertical dotted, solid, and dashed lines indicate
581 the flare start time, peak time, and end time, respectively.

582

583 Figure 2. Example of EUV spectrum observation.

584 The EUV spectrum at the GOES XRS-B peak time (18:52 UT) observed by the
585 SDO/EVE MEGS-A for the M9.9-class flare on January 1, 2014. This EUV spectrum is
586 subtracted non-enhanced value (at 18:00 UT) from the value of each wavelength before
587 the flare as background. The EUV flare lines focused on in this study are indicated as
588 the vertical dotted lines.

589

590 Figure 3. Examples of EUV flare line light curves.

591 The light curves of each EUV flare line (Fe VIII, Fe XV, Fe XVI, Fe XVIII, Fe XX, and

592 He II from the top to bottom panels) observed by the SDO/EVE MEGS-A for the M9.9-
593 class flare on January 1, 2014. The solid lines indicate the observed values with 10 s
594 cadence. The dotted lines indicate the 110 s running average values of the observed
595 data. The 3 min average values (18:00 – 18:03) during the non-enhanced around top of
596 the hour before the flare are subtracted from each light curve as background. Each
597 vertical dotted line indicates the flare start time, peak time, and end time, respectively,
598 from left to right. The arrows indicate the peak time for each EUV flare line.

599

600 Figure 4. Example of fit GOES XRS-B light curve for the M9.9-class flare on January
601 1, 2014.

602 The observed (red) and fit (green) light curves during the M9.9-class flare on January 1,
603 2014 using the Gauss-Newton method.

604

605 Figure 5. Example of flare ribbon observation.

606 The flare ribbon observation by the SDO/AIA 1600 Å for the M9.9-class flare on

607 January 1, 2014. The yellow contour indicates the region with an intensity 40 times

608 greater than the standard deviation of the quiet region. The red arrow indicates the

609 ribbon distance defined in this study.

610

611 Figure 6. Calculated results of CANS 1D.

612 The hydrodynamic calculation results with CANS 1D for (a) temperature distribution,

613 (b) density, (c) pressure, and (d) plasma velocity along the loop. The time evolution is

614 represented by the change of the line color from blue to red.

615

616 Figure 7. Observed and reproduced light curves of GOES XRS-A and XRS-B.

617 The dashed and solid lines indicate the reproduced and observed light curve of GOES

618 XRS during the M9.9-class flare on January 1, 2014, respectively. The red and blue

619 lines represent GOES XRS-B and XRS-A, respectively.

620

621 Figure 8. Example of EUV time-integrated spectra during flare.

622 The EUV time-integrated spectra during the flare for the M9.9-class flare on January 1,

623 2014. The dashed red, blue, and solid green lines indicate the calculated spectra of the

624 proposed model, FISM, and observed spectra by SDO/EVE MEGS-A, respectively. The
625 wavelength resolution for FISM is 10 Å; the proposed model and SDO/EVE MEGS-A
626 observation is 1 Å. The arrows indicate the EUV lines focused on in this study.

627

628 Figure 9. Example of EUV flare line light curves.

629 The EUV flare line light curves for the M9.9-class flare on January 1, 2014. The
630 wavelength resolution of the light curves is 10 Å, which is the same as FISM. The
631 panels indicate the light curves of Fe VIII and Fe XX 130 Å (red), Fe XV 280 Å (cyan),
632 Fe XVI 330 Å (purple), Fe XVIII 90 Å (orange), and He II 300 Å (blue) obtained by the
633 SDO/EVE MEGS-A observation (top panel: solid line), the proposed model estimation
634 (middle panel: dashed line), and FISM estimations (bottom panel: dotted line),
635 respectively. The slope of regression and correlation coefficient (CC) for each model
636 are shown at the upper left and bottom right.

637

638 Figure 10. Comparison results of EUV flare line time-integrated irradiance.

639 The relationship between the SDO/EVE MEGS-A observations and the proposed model

640 estimations of the EUV flare time-integrated irradiance for (a) Fe VIII, (b) Fe XV, (c)
641 Fe XVI, (d) Fe XVIII, (e) Fe XX, and (f) He II. In each panel, the solid line indicates
642 the regression of each plot; the dashed line indicates the straight line with slope of “1”.
643 The slope of regression and correlation coefficient (CC) are shown at the bottom right.

644

645 Figure 11. Comparison results of EUV flare band time-integrated irradiance.

646 The relationship between the SDO/EVE MEGS-A observations and proposed model
647 estimations of the EUV flare energies of two wavelength bands for (a) 55 to 355 Å and
648 (b) 55 to 135 Å. The results of the proposed model are plotted in red; FISM results are
649 plotted in blue. In each panel, the solid line indicates the regression of each plot; the
650 dashed line indicates the straight line with slope of “1”, the slope of regression is shown
651 at the upper left and bottom right.

652

653 Figure 12. The comparison results of the EUV flare line rise time.

654 The relationship between the SDO/EVE MEGS-A observations and proposed model
655 estimations of the EUV flare line rise time for the (a) Fe VIII, (b) Fe XV, (c) Fe XVI,

656 (d) Fe XVIII, (e) Fe XX, (f) He II. In each panel, the dashed line indicates the straight

657 line with slope of “1”, the correlation coefficient (CC) is shown at the bottom right.

658

659 Table 1. Comparative parameters for the M9.9-class flare on January 1, 2014.

660

661 Table 2. Flare event list for this study.

Figures

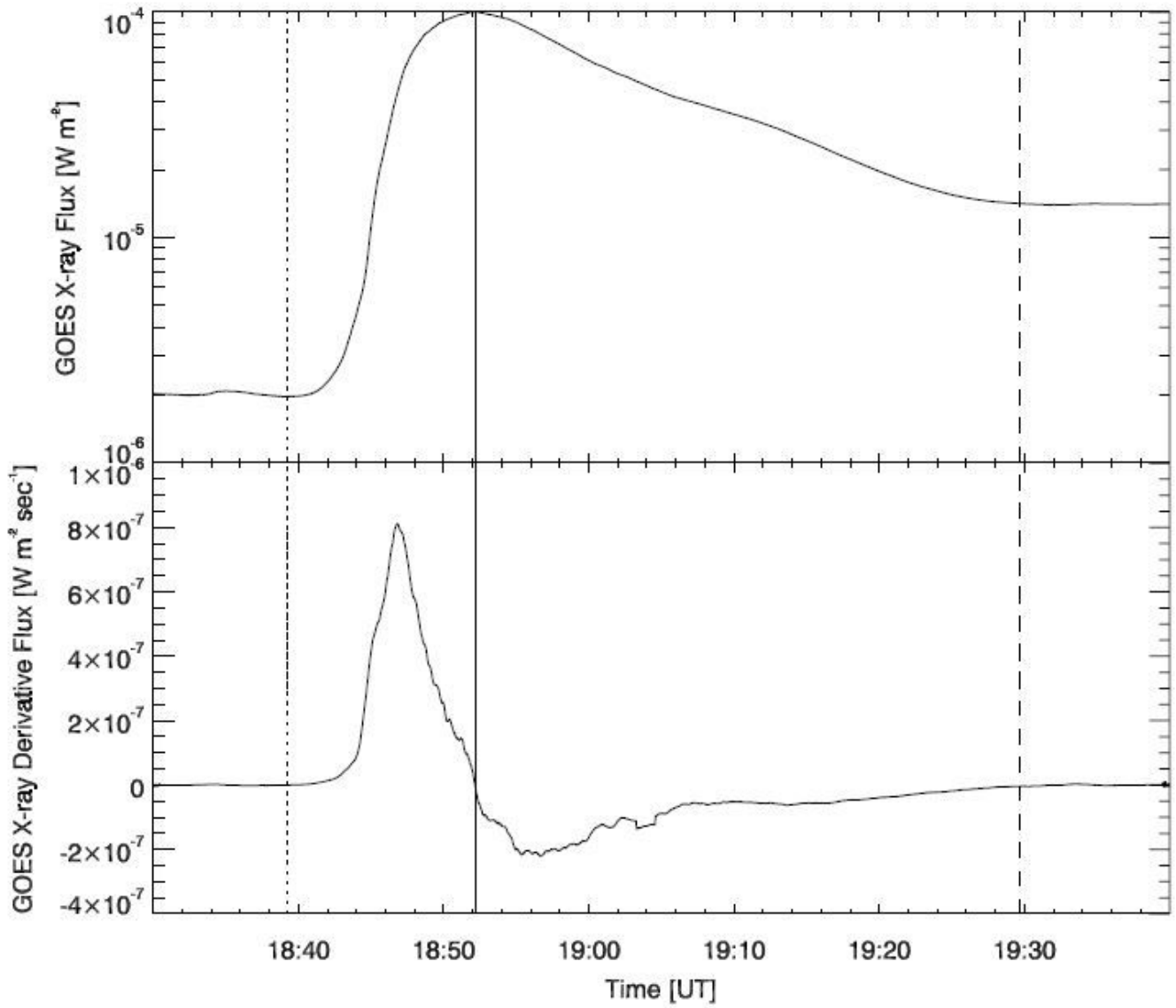


Figure 1

Example of GOES XRS-B observation. The light curve of soft X-ray flux (1 to 8 Å) observed by the GOES XRS-B for the M9.9-class flare on January 1, 2014 (upper panel). The light curve of the soft X-ray time derivative flux (lower panel). The vertical dotted, solid, and dashed lines indicate the flare start time, peak time, and end time, respectively.

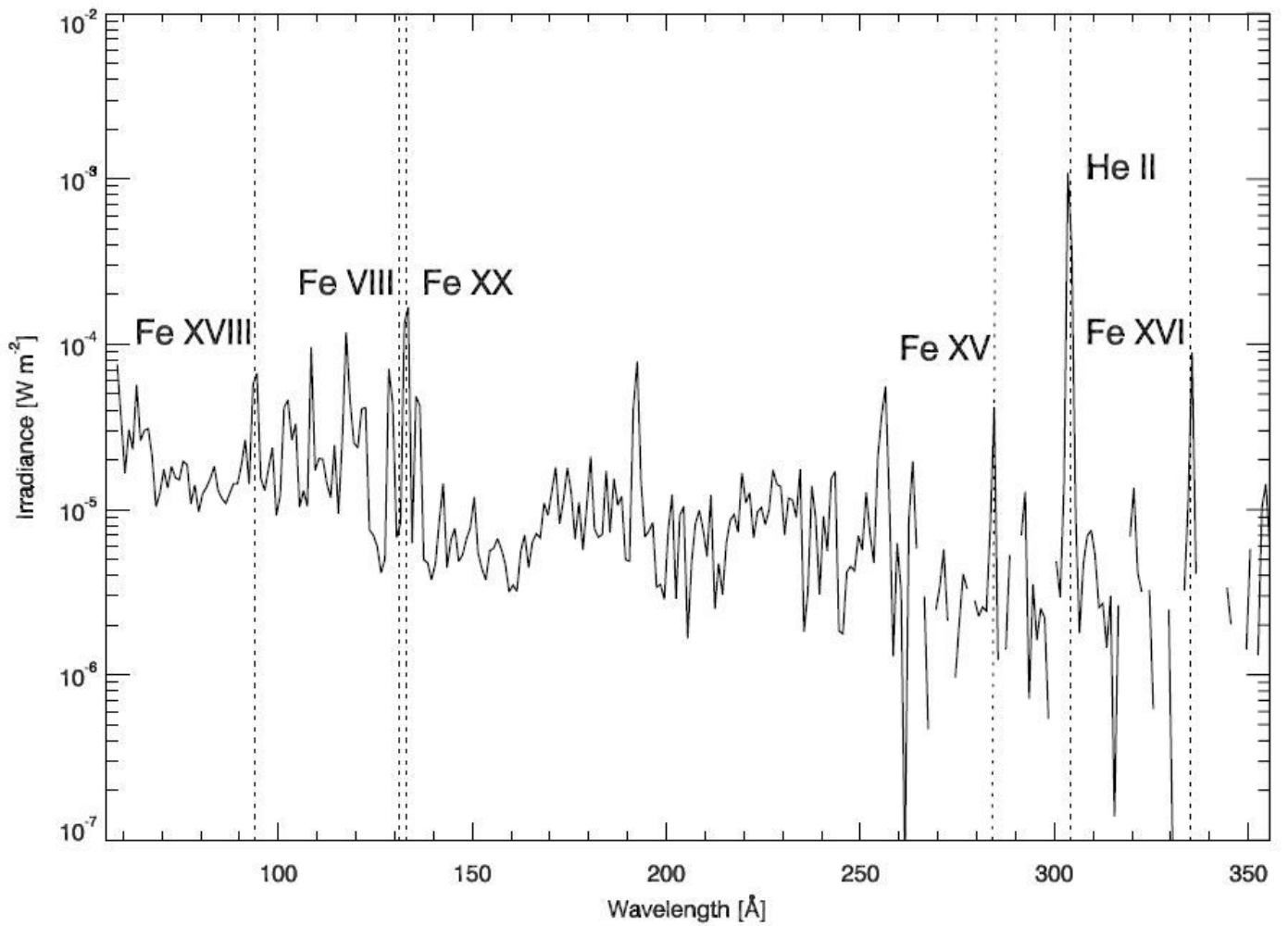


Figure 2

Example of EUV spectrum observation. The EUV spectrum at the GOES XRS-B peak time (18:52 UT) observed by the SDO/EVE MEGS-A for the M9.9-class flare on January 1, 2014. This EUV spectrum is subtracted non-enhanced value (at 18:00 UT) from the value of each wavelength before the flare as background. The EUV flare lines focused on in this study are indicated as the vertical dotted lines.

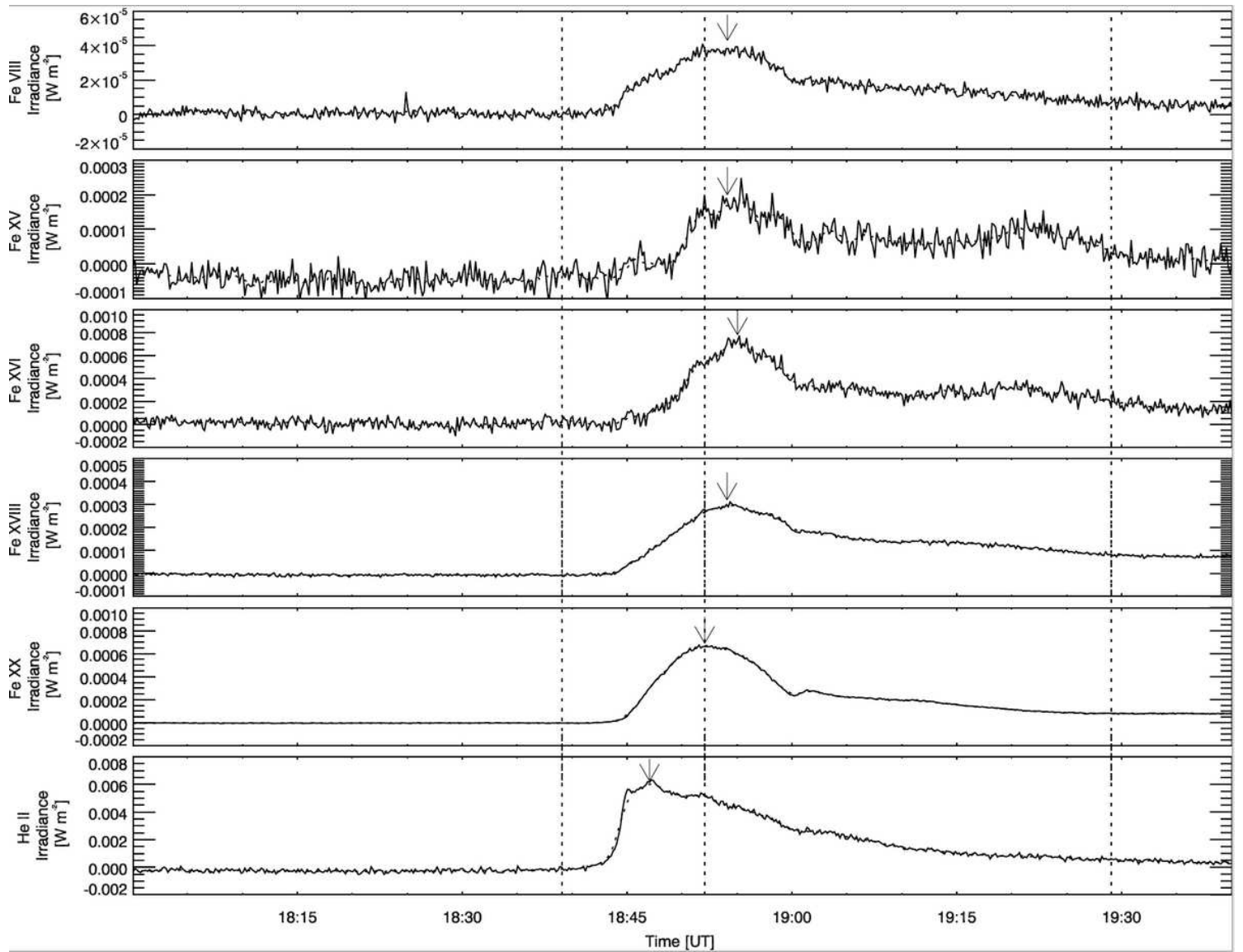


Figure 3

Examples of EUV flare line light curves. The light curves of each EUV flare line (Fe VIII, Fe XV, Fe XVI, Fe XVIII, Fe XX, and He II from the top to bottom panels) observed by the SDO/EVE MEGS-A for the M9.9-class flare on January 1, 2014. The solid lines indicate the observed values with 10 s cadence. The dotted lines indicate the 110 s running average values of the observed data. The 3 min average values (18:00 – 18:03) during the non-enhanced around top of the hour before the flare are subtracted from each light curve as background. Each vertical dotted line indicates the flare start time, peak time, and end time, respectively, from left to right. The arrows indicate the peak time for each EUV flare line.

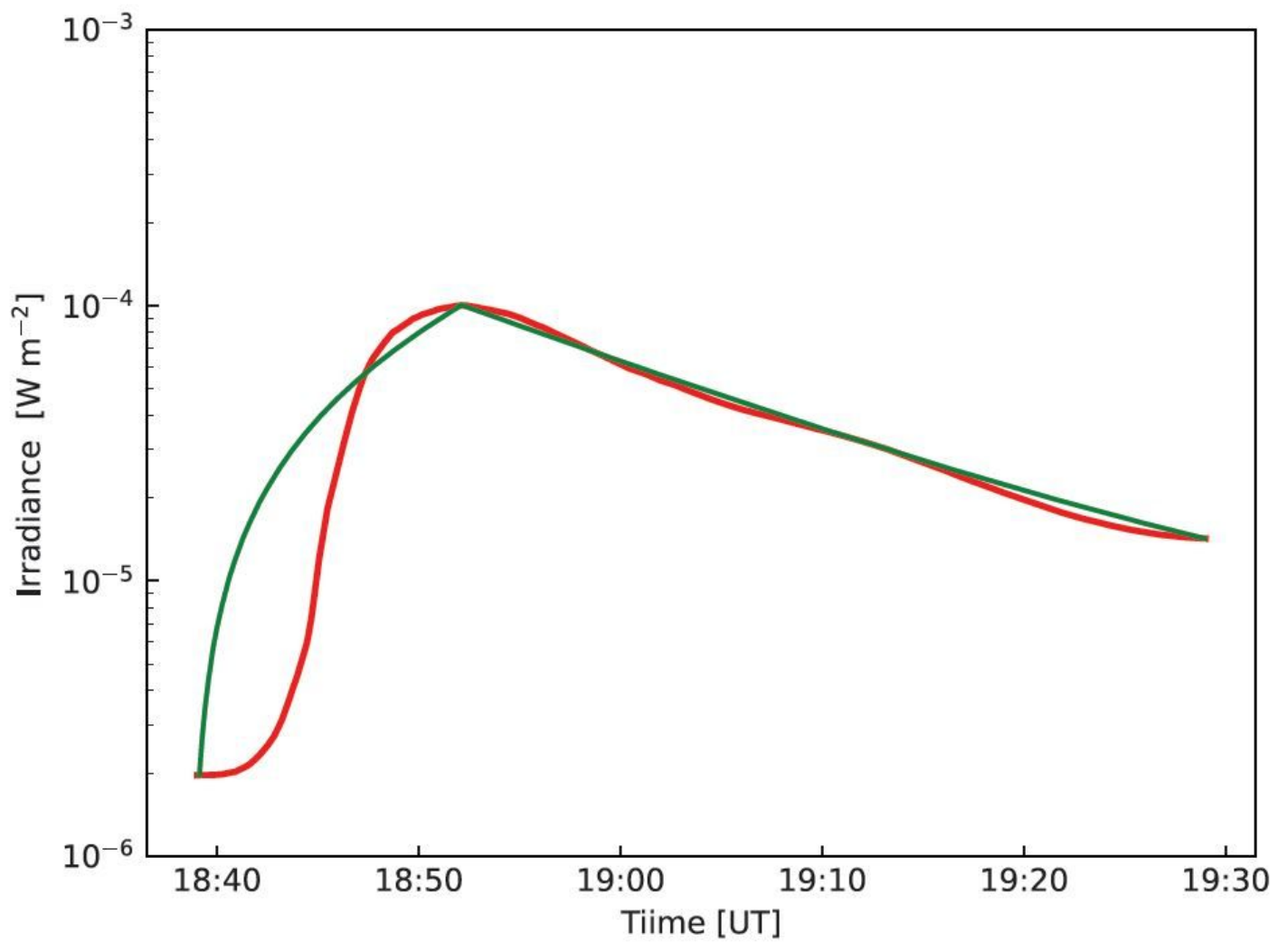


Figure 4

Example of fit GOES XRS-B light curve for the M9.9-class flare on January 1, 2014. The observed (red) and fit (green) light curves during the M9.9-class flare on January 1, 2014 using the Gauss-Newton method.

1-Jan-2014 18:44:16.120 UT

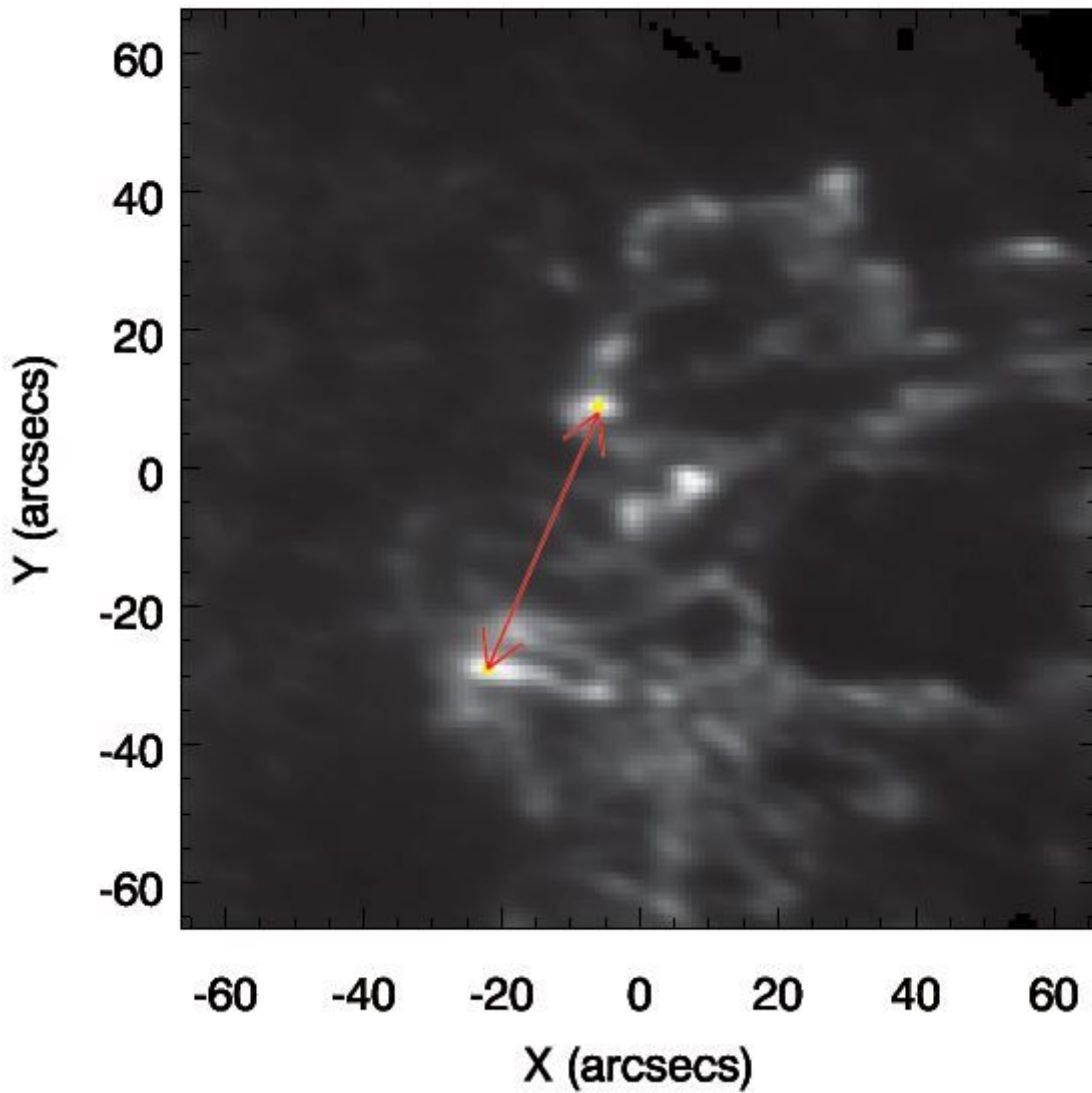


Figure 5

Example of flare ribbon observation. The flare ribbon observation by the SDO/AIA 1600 Å for the M9.9-class flare on January 1, 2014. The yellow contour indicates the region with an intensity 40 times greater than the standard deviation of the quiet region. The red arrow indicates the ribbon distance defined in this study.

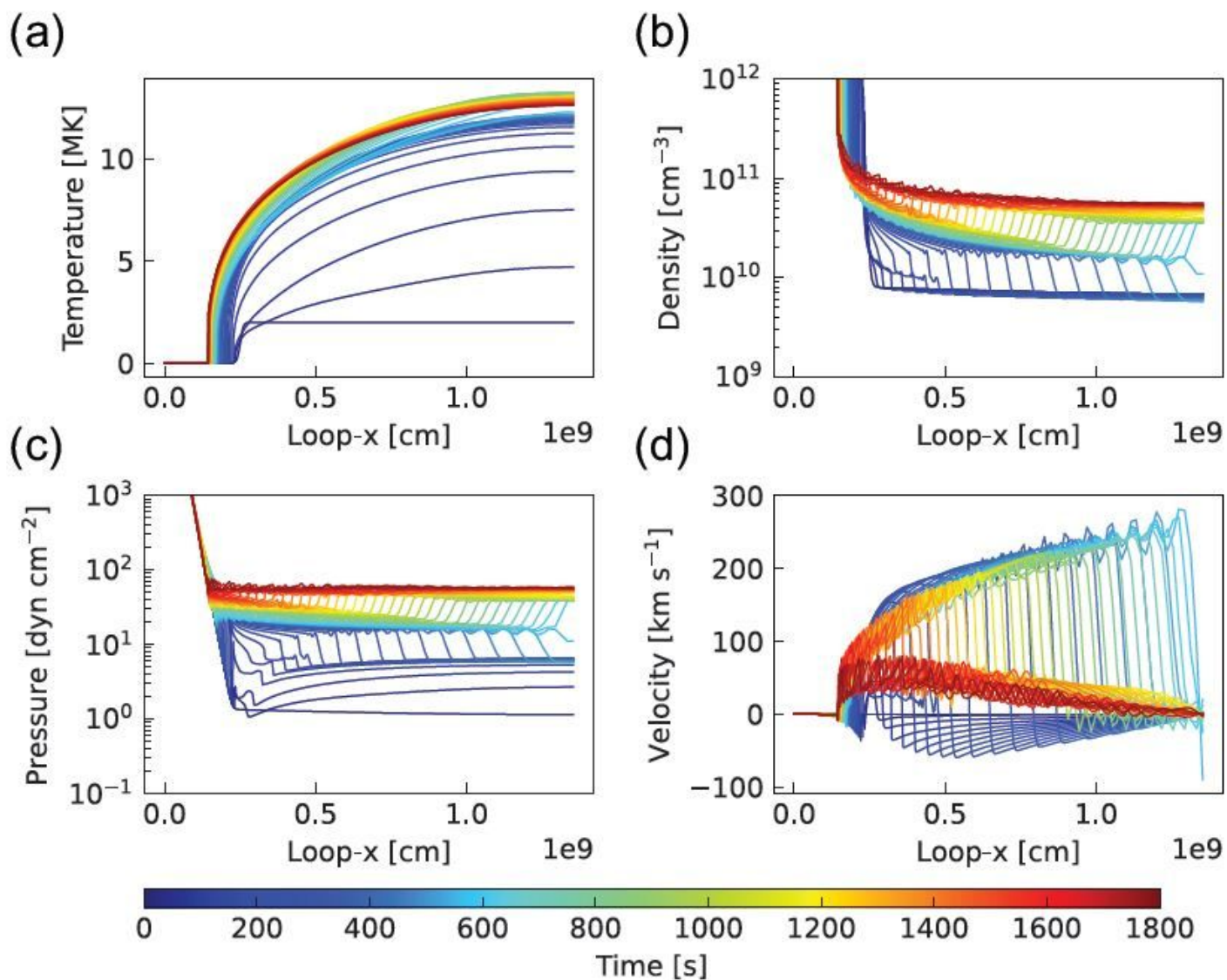


Figure 6

Calculated results of CANS 1D. The hydrodynamic calculation results with CANS 1D for (a) temperature distribution, (b) density, (c) pressure, and (d) plasma velocity along the loop. The time evolution is represented by the change of the line color from blue to red.

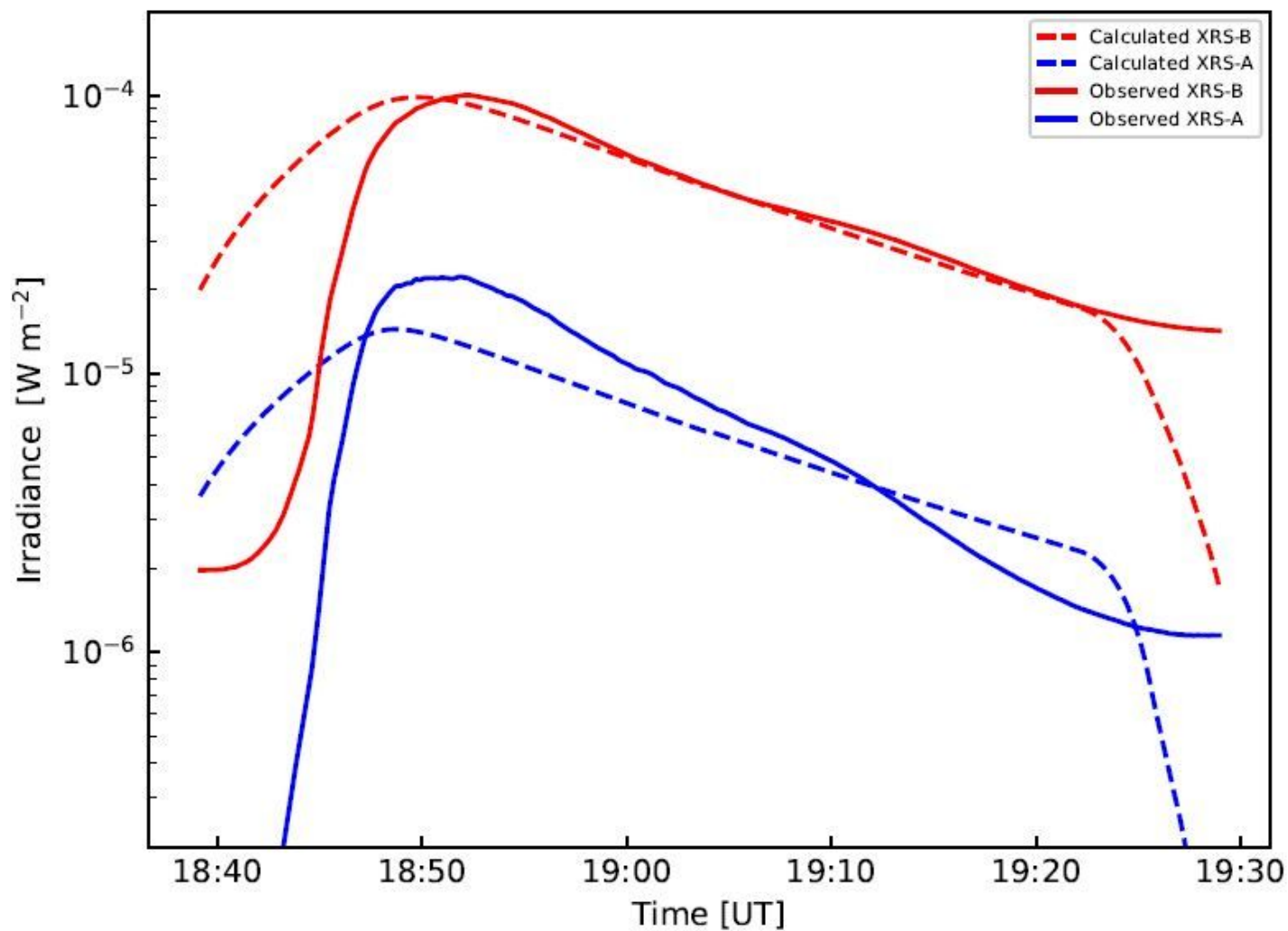


Figure 7

Observed and reproduced light curves of GOES XRS-A and XRS-B. The dashed and solid lines indicate the reproduced and observed light curve of GOES XRS during the M9.9-class flare on January 1, 2014, respectively. The red and blue lines represent GOES XRS-B and XRS-A, respectively.

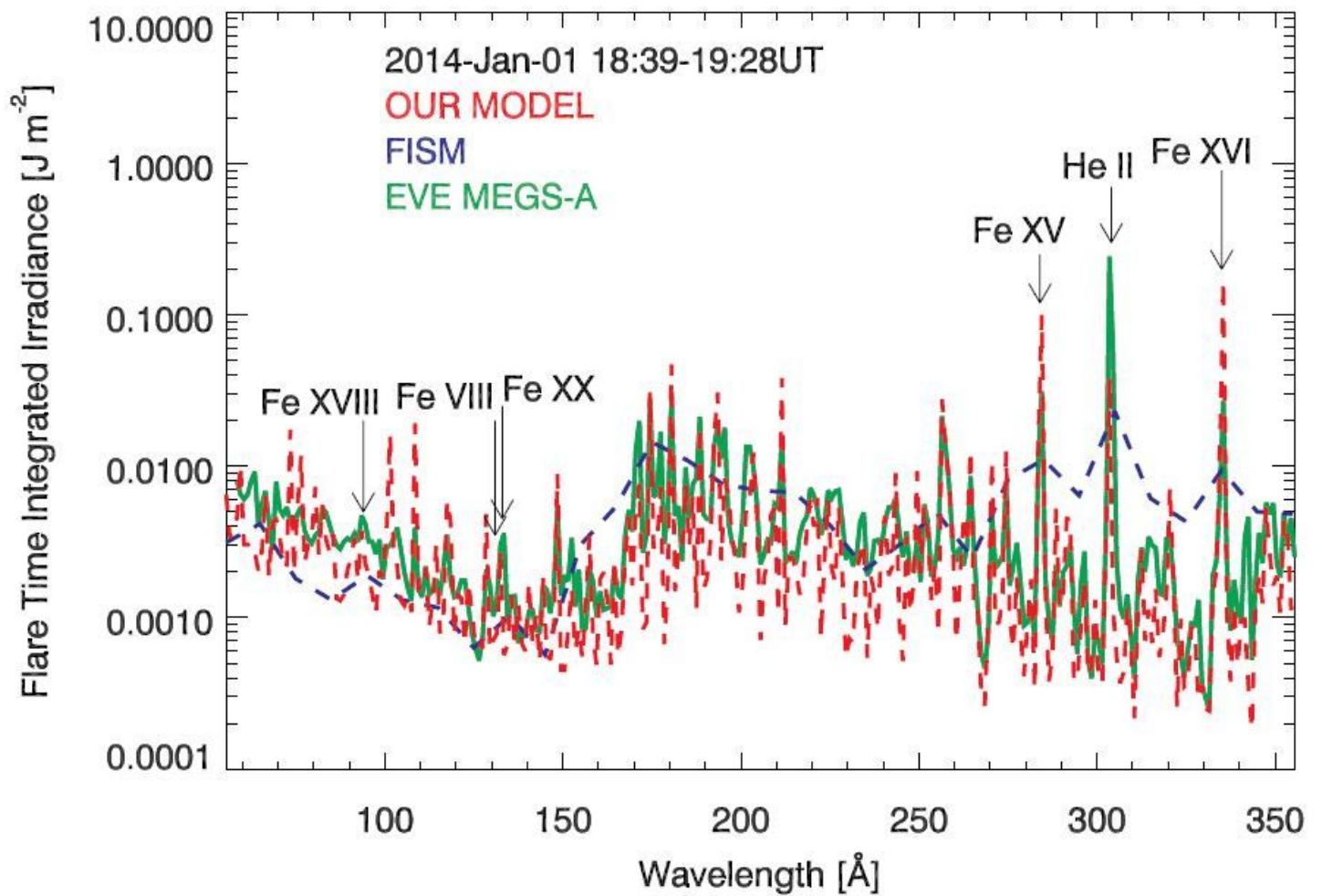


Figure 8

Example of EUV time-integrated spectra during flare. The EUV time-integrated spectra during the flare for the M9.9-class flare on January 1, 2014. The dashed red, blue, and solid green lines indicate the calculated spectra of the proposed model, FISM, and observed spectra by SDO/EVE MEGS-A, respectively. The wavelength resolution for FISM is 10 Å; the proposed model and SDO/EVE MEGS-A observation is 1 Å. The arrows indicate the EUV lines focused on in this study.

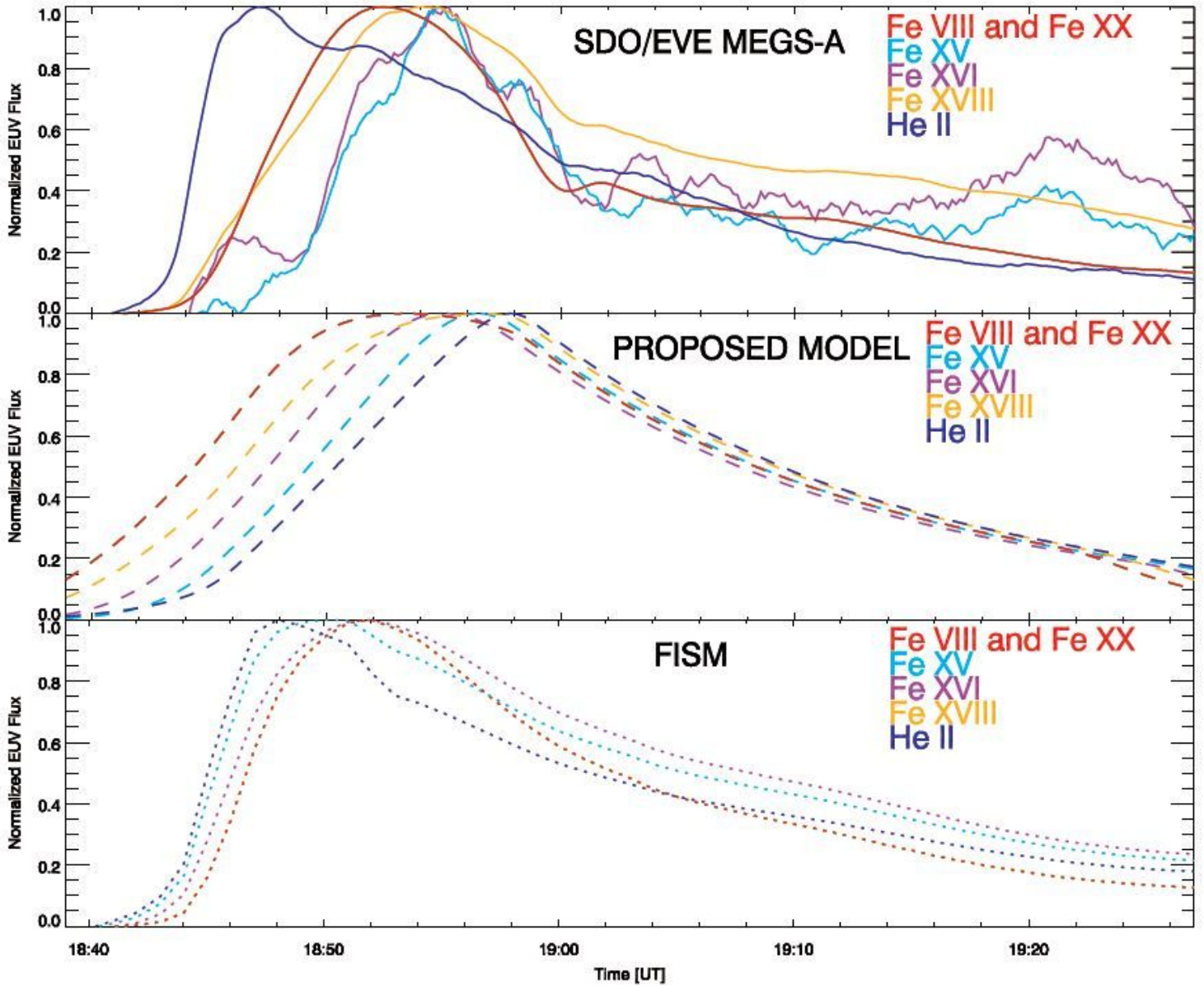


Figure 9

Example of EUV flare line light curves. The EUV flare line light curves for the M9.9-class flare on January 1, 2014. The wavelength resolution of the light curves is 10 \AA , which is the same as FISM. The panels indicate the light curves of Fe VIII and Fe XX 130 \AA (red), Fe XV 280 \AA (cyan), Fe XVI 330 \AA (purple), Fe XVIII 90 \AA (orange), and He II 300 \AA (blue) obtained by the SDO/EVE MEGS-A observation (top panel: solid line), the proposed model estimation (middle panel: dashed line), and FISM estimations (bottom panel: dotted line), respectively. The slope of regression and correlation coefficient (CC) for each model are shown at the upper left and bottom right.

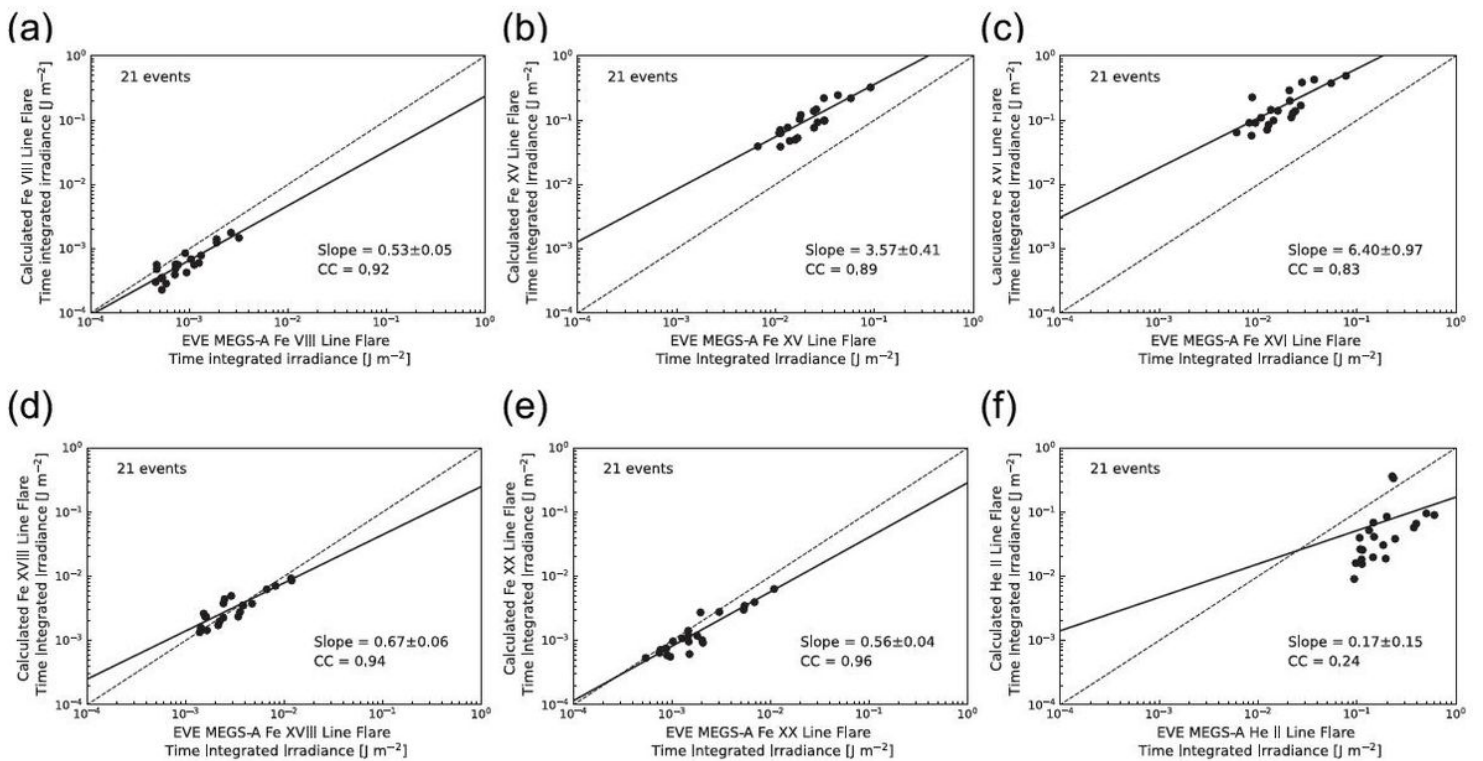


Figure 10

Comparison results of EUV flare line time-integrated irradiance. The relationship between the SDO/EVE MEGS-A observations and the proposed model estimations of the EUV flare time-integrated irradiance for (a) Fe VIII, (b) Fe XV, (c) Fe XVI, (d) Fe XVIII, (e) Fe XX, and (f) He II. In each panel, the solid line indicates the regression of each plot; the dashed line indicates the straight line with slope of “1”. The slope of regression and correlation coefficient (CC) are shown at the bottom right.

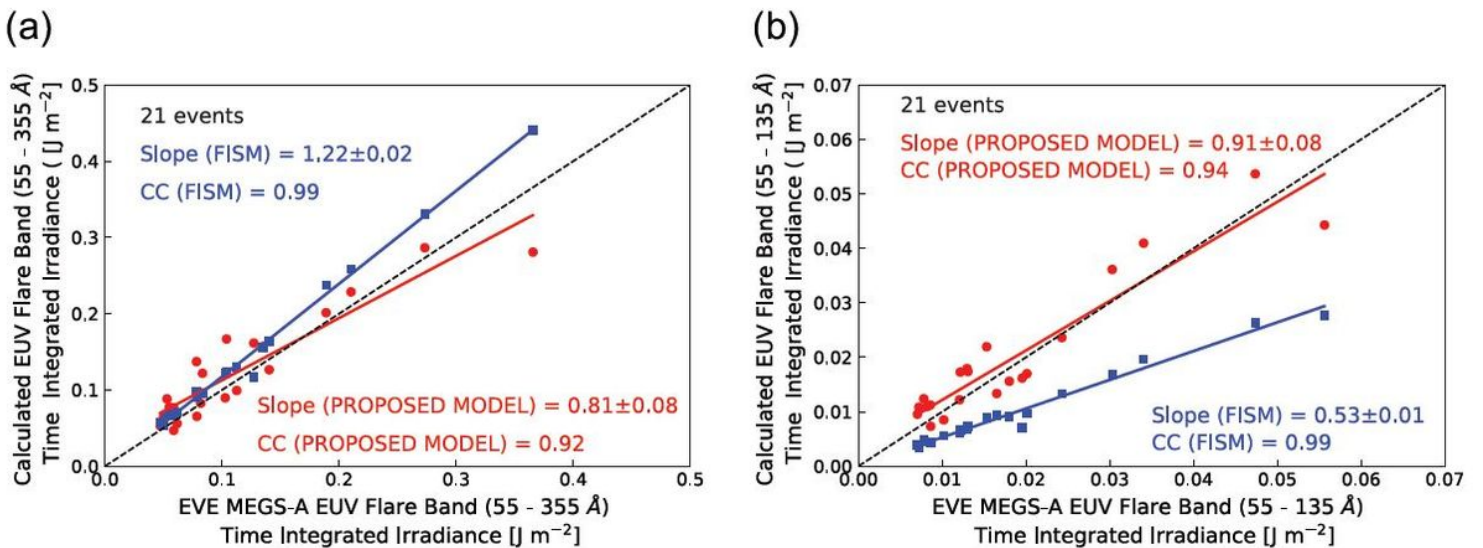


Figure 11

Comparison results of EUV flare band time-integrated irradiance. The relationship between the SDO/EVE MEGS-A observations and proposed model estimations of the EUV flare energies of two wavelength

bands for (a) 55 to 355 Å and (b) 55 to 135 Å. The results of the proposed model are plotted in red; FISM results are plotted in blue. In each panel, the solid line indicates the regression of each plot; the dashed line indicates the straight line with slope of “1”, the slope of regression is shown at the upper left and bottom right.

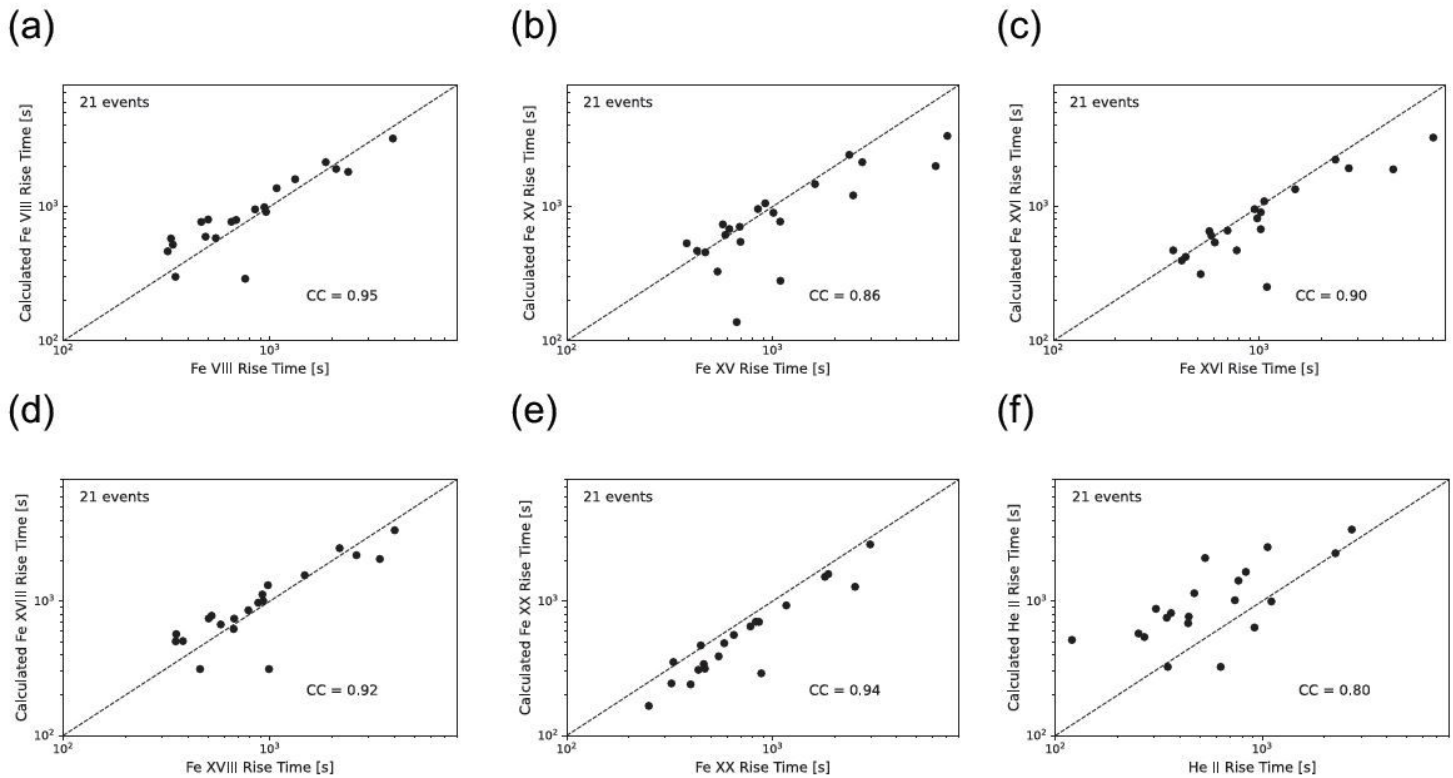


Figure 12

The comparison results of the EUV flare line rise time. The relationship between the SDO/EVE MEGS-A observations and proposed model estimations of the EUV flare line rise time for the (a) Fe VIII, (b) Fe XV, (c) Fe XVI, (d) Fe XVIII, (e) Fe XX, (f) He II. In each panel, the dashed line indicates the straight line with slope of “1”, the correlation coefficient (CC) is shown at the bottom right.

Supplementary Files

This is a list of supplementary files associated with this preprint. Click to download.

- [table1.xls](#)
- [table2.xls](#)
- [graphicabst.png](#)